Research Article

Nano Research
2022, 15(5): 4668–4676

ISSN 1998-0124 CN 11-5974/O4
https://doi.org/10.1007/s12274-022-4110-3

Anisotropic electrical properties of aligned $PtSe_2$ nanoribbon arrays grown by a pre-patterned selective selenization process

Huaipeng Wang[1,§], Zhifang Liu[2,§], Yilin Sun[3] (✉), Xiaofan Ping[2], Jianlong Xu[4], Yingtao Ding[3], Haowen Hu[5], Dan Xie[1] (✉), and Tianling Ren[1] (✉)

[1] *School of Integrated Circuits, Beijing National Research Center for Information Science and Technology (BNRist), Tsinghua University, Beijing 100084, China*
[2] *Department of Chemistry, Tsinghua University, Beijing 100084, China*
[3] *School of Integrated Circuits and Electronics, Beijing Institute of Technology, Beijing 100081, China*
[4] *Institute of Functional Nano & Soft Materials (FUNSOM), Jiangsu Key Laboratory for Carbon-Based Functional Materials & Devices, Soochow University, Suzhou 215123, China*
[5] *State Key Lab of New Ceramics and Fine Processing, School of Materials Science and Engineering, Tsinghua University, Beijing 100084, China*
[§] *Huaipeng Wang and Zhifang Liu contributed equally to this work.*

Received: 15 November 2021 / **Revised:** 17 December 2021 / **Accepted:** 23 December 2021

ABSTRACT

This study proposes a feasible and scalable production strategy to naturally obtain aligned platinum diselenide ($PtSe_2$) nanoribbon arrays with anisotropic conductivity. The anisotropic properties of two-dimensional (2D) materials, especially transition-metal dichalcogenides (TMDs), have attracted great interest in research. The dependence of physical properties on their lattice orientations is of particular interest because of its potential in diverse applications, such as nanoelectronics and optoelectronics. One-dimensional (1D) nanostructures facilitate many feasible production strategies for shaping 2D materials into unidirectional 1D nanostructures, providing methods to investigate the anisotropic properties of 2D materials based on their lattice orientations and dimensionality. The natural alignment of zigzag (ZZ) $PtSe_2$ nanoribbons is experimentally demonstrated using angle-resolved polarized Raman spectroscopy (ARPRS), and the selective growth mechanism is further theoretically revealed by comparing edges and edge energies of different orientations using the density functional theory (DFT). Back-gate field-effect transistors (FETs) are also constructed of unidirectional $PtSe_2$ nanoribbons to investigate their anisotropic electrical properties, which align with the results of the projected density of states (DOS) calculations. This work provides new insight into the anisotropic properties of 2D materials and a feasible investigation strategy from experimental and theoretical perspectives.

KEYWORDS

$PtSe_2$, scalable production, anisotropic properties, nanoribbons, density functional theory

1 Introduction

The family of two-dimensional (2D) layered transition-metal dichalcogenides (TMDs) has been greatly expanded to cover semiconductors (e.g., MoS_2 [1, 2] and WSe_2 [3]) and semimetals (WTe_2) [4], which exhibit diverse electrical and optical properties such as thickness-dependent strong light–matter interaction [5, 6], semiconductor-to-metal transition [7], electrical properties [8], and newly observed in-plane and out-of-plane ferroelectricity [9]. These outstanding properties have promoted a wide range of TMD applications in nanoelectronics and optoelectronics, including logic circuits, memory cells, and photodetectors [10–12]. Interestingly, great efforts have been devoted to clarifying the dependence of the physical properties of TMDs on their lattice orientations, especially for zigzag (ZZ) and armchair (AC) lattice orientations. This has provoked heated discussion on the anisotropic properties of magnetism [13], thermoelectric behavior [14], mechanical strength [15], and light-matter interaction [16]. For example, a polarized photo response can be achieved by breaking the crystal symmetry of monolayer MoS_2, generating novel anisotropic optoelectronic properties for achieving near-infrared polarization imaging and sensing systems [17]. Similar anisotropic electrical and optical properties have been theoretically and experimentally demonstrated in few-layer black phosphorus, where a high Hall mobility of 1,000 $cm^2 \cdot V^{-1} \cdot S^{-1}$ was obtained along the light effective mass directions [18, 19]. Although the anisotropic properties of TMDs contribute to the development of novel nanoelectronics, it is still a great challenge to directly judge the orientation of TMDs from their 2D morphology without resorting to complex characterization methods. In addition, the lack of efficient production methods for unidirectional TMD nanostructures hinders their applications in advanced electronics and optoelectronics.

A one-dimensional (1D) nanostructure with nanoribbons or nanobelts as typical morphological features provides a unique opportunity to investigate the electrical and optical properties based on their dimensionality [20]. Therefore, shaping 2D

Address correspondence to Yilin Sun, sunyl@bit.edu.cn; Dan Xie, xiedan@tsinghua.edu.cn; Tianling Ren, rentl@tsinghua.edu.cn

nanoflakes into 1D nanostructures, such as AC or ZZ MoS_2 nanoribbons, is a feasible strategy to obtain unidirectional crystal orientation of TMDs with anisotropic properties [21, 22]. Recently, a variety of orientation-selective productions of 1D nanostructures have been proposed, which has paved the way for research on the anisotropic properties of TMDs from theoretical prediction to experimental verification. The reported production of anisotropic 1D nanostructures can be divided into physical etching and chemical cutting. The former involves complex micro-nano processing assisted with angle-resolved polarized Raman spectroscopy (ARPRS) characterization, where the crystal orientation of 2D nanoflakes is first determined by ARPRS. Subsequently, the morphology of nanoribbons or nanobelts is defined using a graphical electron-beam lithography (EBL) process, which is followed by an etching technology to finally form the unidirectional 1D nanostructures [23–25]. This EBL-assisted physical etching method can precisely control the crystal orientation of the as-fabricated 1D nanostructure. However, its application is limited by the processing complexity, which relies on the polarized Raman prior to the EBL, and a lower yield due to the inefficiency of mechanical exfoliation, which is not suitable for scalable production. Chemical cutting is proposed to produce a scalable production and create 1D nanostructures from the bulk form of 2D materials using electrochemical exfoliation under solution conditions [26, 27]. This method achieves the scalable production of 1D nanostructures, but its uniformity, quality, and controllability are still issues that require urgent solutions. Moreover, unexpected impurities or functional groups can be easily introduced during the exfoliation process, which significantly degrades the performance of the as-fabricated 1D nanostructures.

This study proposes a simple and scalable production method for aligned platinum diselenide ($PtSe_2$) nanoribbon arrays, which are directly formed from the selenization of pre-defined Pt nanoribbons. $PtSe_2$ is an interesting new member of the TMD family that exhibits a tunable bandgap from 0 to 1.2 eV by decreasing its thickness and controllable semiconductor-to-metal transition [28, 29]. A simple *in situ* synthesis method is proposed to directly deposit Se on a Pt substrate to form 2D $PtSe_2$, which is distinct from conventional TMDs that use chemical vapor deposition. This is known as a selenization process, which is widely applied to build high-mobility field-effect transistors (FETs) and broadband photodetectors, demonstrating the great potential of $PtSe_2$ to integrate into large-scale nanoelectronics [29–31]. However, few studies have discussed the scalable production of $PtSe_2$ nanoribbons and their physical properties, especially the anisotropic properties.

This study focuses on the ZZ $PtSe_2$ nanoribbons that can be naturally obtained along the long axis direction of nanoribbons during selenization. A set of characterizations, such as high-resolution transmission electron microscopy (HRTEM) and ARPRS, are conducted to confirm the unidirectional crystal orientation of the as-fabricated $PtSe_2$ nanoribbons. The results of theoretical calculations reveal the underlying mechanism behind this preferred oriented growth and align with the anisotropic conductivity observed in $PtSe_2$ nanoribbon-based FETs. The above results provide a feasible strategy for fabricating unidirectional $PtSe_2$ nanoribbon arrays using a one-step simple selenization process and pave a new way to explore the anisotropic physics of TMDs.

2 Results and discussion

2.1 Production of $PtSe_2$ nanoribbons

A feasible pattern strategy for $PtSe_2$ was proposed, as shown in Fig. 1(a) and Fig. S1(a) in the Electronic Supplementary Material (ESM). A series of lithography methods, e.g., photolithography, direct laser writing, and EBL, could be utilized to generate the patterns of nanoribbon arrays. Herein, to control the morphology more precisely, EBL was chosen to generate the nanoribbon patterns. Briefly, the photoresist spin-coated on the SiO_2 substrate was initially patterned using EBL. Then, a thin Pt layer (~ 2.2 nm) was deposited onto the patterned substrate using electron-beam evaporation, as shown in Fig. S1(b) in the ESM, followed by a simple selenization process to produce $PtSe_2$ nanoribbon arrays with an average thickness of ~ 3.5 nm. The color change of the surface indicates a transmission from Pt to $PtSe_2$ with increased

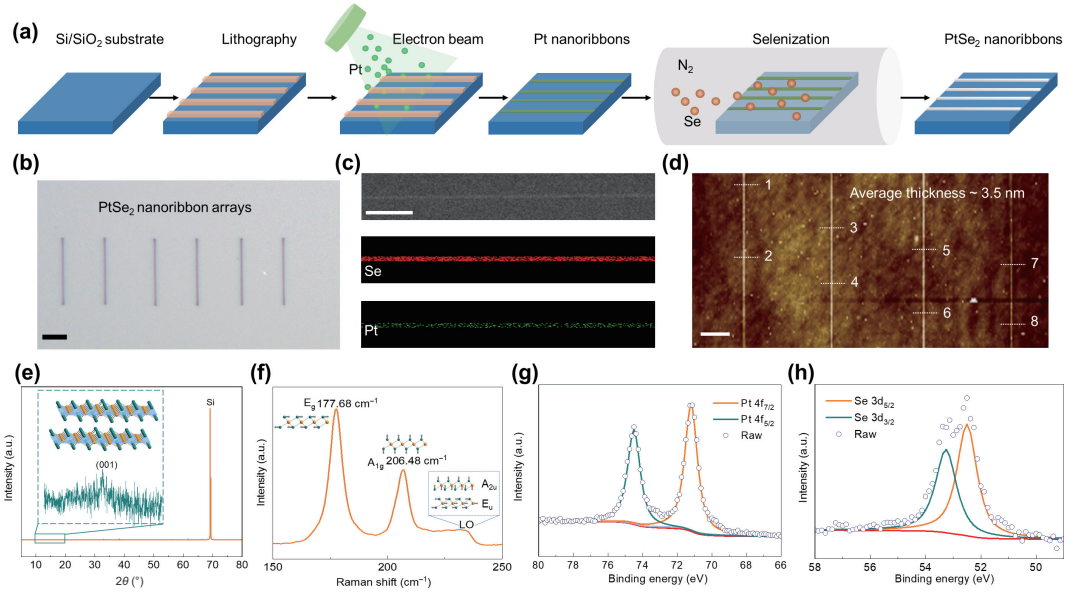

Figure 1 Production and characterizations of $PtSe_2$ nanoribbons. (a) Schematic of the production process of $PtSe_2$ nanoribbon arrays. (b) SEM image of $PtSe_2$ nanoribbon arrays. Scale bar: 1 μm. (c) SEM mapping of a single $PtSe_2$ nanoribbon, indicating the Se and Pt element distribution. Scale bar: 1 μm. (d) AFM image of $PtSe_2$ nanoribbon arrays with a width of 100 nm and thickness of ~ 3.5 ± 0.3 nm from 8 points on the nanoribbon arrays. Scale bar: 1 μm. (e) XRD spectra of the $PtSe_2$ nanoribbons onto the SiO_2 substrate. Inset: enlarged XRD peak for crystallographic plane (001) of $PtSe_2$. (f) Raman spectra of $PtSe_2$ nanoribbon with three Raman active modes: E_g, A_{1g}, and LO. Inset: Raman vibration of each mode. (g) and (h) Se and Pt XPS spectra, respectively, with an atom ratio between Se and Pt of ~ 1.92.

thickness, as shown in Figs. S1(a) and S2 in the ESM. The selenization was carried out for Pt arrays with different thicknesses and a proportional relationship between the Pt thickness and the corresponding $PtSe_2$ thickness was fitted, as shown in Fig. S1(c) in the ESM. The perpendicular nanoribbon arrays were successfully produced with equidistant spacing, as shown in Fig. 1(b). Scanning electron microscopy (SEM) images and the corresponding energy dispersive X-ray spectroscopy (EDS) showed that the $PtSe_2$ nanoribbons had uniform element distribution, which was also confirmed by HRTEM and Raman mapping, as shown in Fig. 1(c) and Figs. S3 and S4 in the ESM. Atomic force microscopy (AFM) was conducted to estimate the thickness of the as-fabricated nanoribbons. We chose 8 points on the nanoribbons, indicating average thickness of ~ 3.5 ± 0.3 nm and corresponded to five layers, as shown in Fig. 1(d) [32]. Single layer $PtSe_2$ has been reported to include a Pt layer sandwiched between two Se layers, forming a trigonal structure accumulating along the [001] direction of the D^3_{3d} ($P\bar{3}m1$) space group [33]. From the X-ray diffraction (XRD) results, a weak and broad peak was observed at approximately 17.4°, corresponding to the (001) plane of $PtSe_2$, as shown in the inset of Fig. 1(e) [31]. Notably, according to the Scherrer equation, the enlarged half-width value of the (001) peak indicated that the as-fabricated $PtSe_2$ nanoribbons were composed of few-layer structures. In addition, a sharp peak was observed at ~ 69°, indicating the existence of a Si substrate, as shown in Fig. 1(e) [31]. Similar to other TMDs, $PtSe_2$ has two main Raman modes: E_g (177.68 cm^{-1}) and A_{1g} (206.48 cm^{-1}), which correspond to the in-plane and out-of-plane vibration modes of Se atoms, respectively, as shown in Fig. 1(f). The intensity of the A_{1g} mode was less than that of the E_g mode due to the fact that the in-plane vibrations produced a larger Raman intensity compared with the out-of-plane vibrations in few-layer $PtSe_2$, as shown in Fig. 1(f) and Fig. S5 in the ESM. Another blunt peak of the longitudinal optical (LO) mode at ~ 240 cm^{-1} was often observed in thin samples [31, 34], which was attributed to the combination of out-of-plane A_{2u} and in-plane E_u vibrations [34, 35]. It is known that the edge effect influences the Raman shift and intensity of anisotropic nanoribbons. Raman spectra at different locations on the nanoribbon (left, middle, and right) showed no changes in shifts or intensities, as shown in Fig. S5 in the ESM. Micro-zone X-ray photoelectron spectroscopy (XPS) measurements of the nanoribbon arrays were taken to further evaluate the elemental valence states and purity of the samples. Si, O, and C are the only elements from the substrate or unavoidable impurities existing in the XPS survey, as shown in Fig. S6 in the ESM. The XPS spectra of the Pt 4f orbital for $PtSe_2$ showed two main peaks at approximately 71.1 eV (Pt $4f_{7/2}$) and 74.5 eV (Pt $4f_{5/2}$), as shown in Fig. 1(g). The Se 3d orbital also showed two peaks at 52.5 eV (Se $3d_{5/2}$) and 53.3 eV (Se $3d_{3/2}$), as seen in Fig. 1(h) [31]. The atomic ratio of Se to Pt was calculated to be 1.92 according to the area ratio of Pt 4f and Se 3d, indicating that a few Se vacancies were unavoidably introduced during the production of $PtSe_2$ [36].

2.2 Characterization of $PtSe_2$ nanoribbons

$PtSe_2$ possesses a natural anisotropic atomic structure, including ZZ and AC directions corresponding to [100] and [010] crystallographic directions, respectively, as shown in Fig. 2(a).

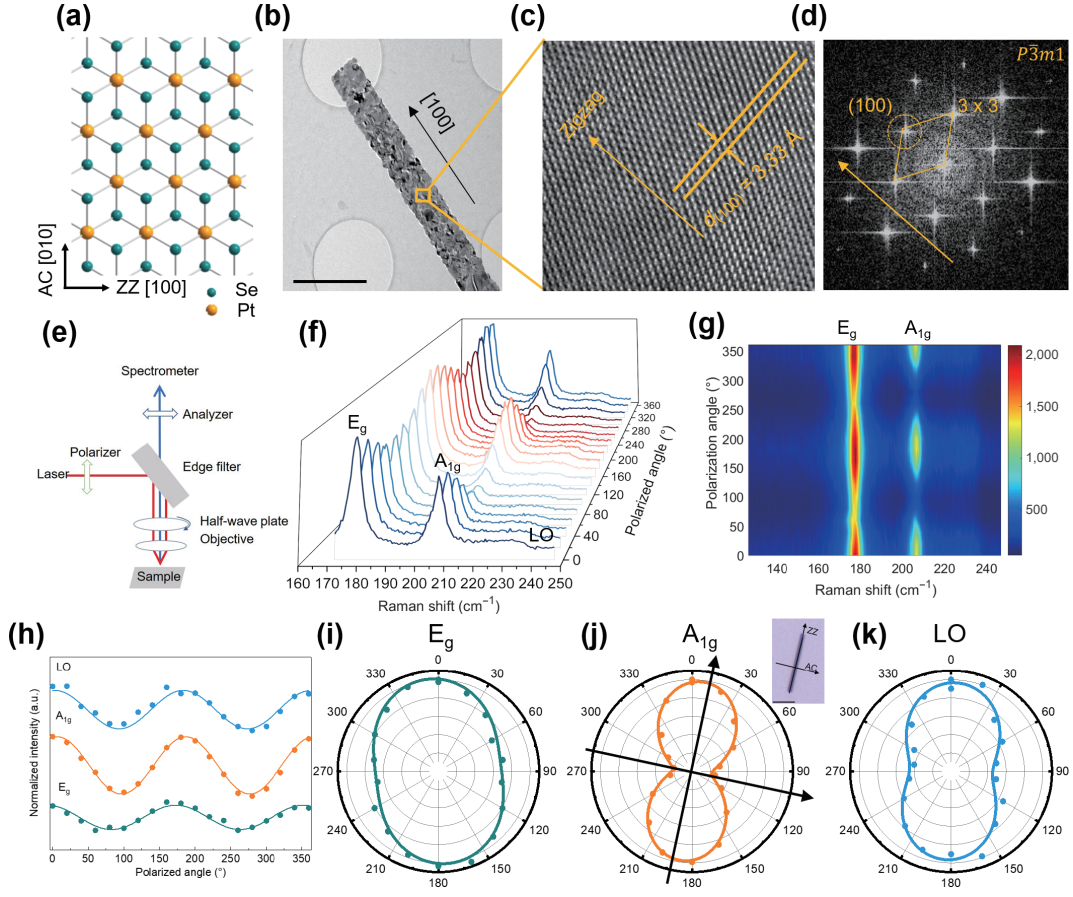

Figure 2 Anisotropic structures of $PtSe_2$ nanoribbons. (a) Top view of atomic structures of $PtSe_2$, indicating the orthogonal ZZ and AC directions. (b) TEM image of $PtSe_2$ nanoribbon. Scale bar: 1 μm. (c) HRTEM image of the yellow $PtSe_2$ nanoribbon region from (b). (d) Corresponding FFT patterns of (c). The (100) plane is circled and indicates a $P\bar{3}m1$ space group. (e) Schematic of the ARPRS test by rotating the polarized light. (f) ARPRS with different angles ranging from 0°–360° with spacing of 20°. (g) ARPRS mapping spectra from (f). (h) Measured and fitting ARPRS signal of the nanoribbon of three modes as a function of the rotation angle. (i)–(k) Polarization diagrams of intensities of E_g, A_{1g}, and LO active modes from (h), respectively. Inset: optical image of $PtSe_2$ nanoribbon. Scale bar: 5 μm.

Transmission electron microscopy (TEM), HRTEM, and ARPRS methods were conducted to explore the crystallographic orientation of $PtSe_2$. The TEM of $PtSe_2$ nanoribbons showed that they have a rough surface with some crystal islands, as shown in Fig. 2(b). This might be caused by the suppression of the diffusion of reactive atoms during the natural cooling of the growth process [37]. Furthermore, HRTEM and selected area electron diffraction (SAED) results indicated that the $PtSe_2$ nanoribbons are polycrystalline rather than single crystalline (Fig. S7 in the ESM), which is similar to previous reports [31]. No obvious lattice defects were observed in the large-area HRTEM image, as shown in Fig. S8 in the ESM. Fast Fourier transform (FFT) patterns demonstrated that the crystal zone axis from Fig. 2(c) was along the [100] direction (i.e., ZZ direction) in Fig. 2(d), which was perpendicular to the plane (100) in trigonal systems.

To further study the anisotropic structure of the as-fabricated $PtSe_2$ nanoribbons, ARPRS was carried out to nondestructively identify the ZZ and AC crystallographic directions of $PtSe_2$ nanoribbons by rotating the polarized light, as shown in Fig. 2(e). The ARPRS of $PtSe_2$ nanoribbons at different polarization angles of scattered light ranging from 0° to 360° showed that the intensities of the three Raman modes (E_g, A_{1g}, and LO) varied periodically with different amplitudes, as shown in Figs. 2(f)–2(h), respectively. To distinguish the crystal direction more clearly, the polar plots of the E_g, A_{1g}, and LO modes were fitted at 177.7, 206.5, and 229.0 cm^{-1}, as shown in Figs. 2(i)–2(k), respectively. It is known that there are six phonon modes at the Brillouin zone center, and the irreducible representation can be expressed as [38]

$$\Gamma = A_{1g} + E_g + 2A_{2u} + 2E_u \quad (1)$$

Among these vibrational modes, A_{1g} and E_g are Raman-active modes. A_{2u} and E_u are infrared active modes, together forming the LO mode. It was noted that the E_g mode was doubly degenerated and could be expressed by two Raman tensors, E_{gx} and E_{gy}. The Raman-active modes of $PtSe_2$ can be written as [39, 40]

$$\boldsymbol{R}(E_{gx}) = \begin{bmatrix} c & 0 & 0 \\ 0 & -c & d \\ 0 & d & 0 \end{bmatrix} \quad (2)$$

$$\boldsymbol{R}(E_{gy}) = \begin{bmatrix} 0 & -c & -d \\ -c & 0 & 0 \\ -d & 0 & 0 \end{bmatrix} \quad (3)$$

$$\boldsymbol{R}(A_{1g}) = \begin{bmatrix} a & 0 & 0 \\ 0 & a & 0 \\ 0 & 0 & b \end{bmatrix} \quad (4)$$

where $\boldsymbol{R}$ is the Raman tensor. Then, two polarization vectors of incident light and scattering light, $\boldsymbol{e}_i$ and $\boldsymbol{e}_s$, were defined as (cosθ, sinθ, 0) and (100), respectively [40]. θ represents the polarization angle between $\boldsymbol{e}_i$ and $\boldsymbol{e}_s$. Thus, the Raman scattering efficiency of the E_g and A_{1g} modes calculated from $\sum(|\boldsymbol{e}_i \times R \times \boldsymbol{e}_s|)^2$ can be expressed as

$$I_{E_g} \propto c^2 \quad (5)$$

$$I_{A_{1g}} \propto a^2 \cos^2\theta \quad (6)$$

E_g was independent of the polarized angle and changed periodically, as shown in Fig. 2(i). This is different from previous reports [38, 40] and might be due to the effect of the polycrystalline SiO_2 substrate. The A_{1g} Raman-active mode was then chosen to determine the edge type. The A_{1g} signal was strongest when scattered light was along the ZZ direction of the $PtSe_2$ nanoribbon, which is consistent with the optical image of the $PtSe_2$ nanoribbon shown in Fig. 2(j). Thus, similar to MoS_2 [41], the relative largest or smallest A_{1g} mode intensity corresponded to the ZZ or AC direction of the $PtSe_2$ nanoribbon, respectively. ARPRS tests based on the other $PtSe_2$ nanoribbons prepared by our method were also conducted, indicating that all the nanoribbons tested showed crystal orientation of ZZ direction (Fig. S9 in the ESM). In summary, the HRTEM and ARPRS results fully demonstrated that the $PtSe_2$ nanoribbons were naturally grown along the ZZ direction during the selenization of pre-patterned Pt nanoribbons. Furthermore, these results indicate that the anisotropic lattice orientation can be fundamentally and technically applied [42].

2.3 First-principle calculations

First-principle calculations using density functional theory (DFT) were performed to investigate the surface energy of different nanoribbon edges and reveal the underlying mechanism for the natural orientation-selective growth of $PtSe_2$ nanoribbons with anisotropic atomic structures. There were total of three types of edges, as shown in Fig. 3(a). Different edges formed for ZZ nanoribbons (ZNRs) when $PtSe_2$ sheets were cut off along the line where the Pt or Se atoms were aligned, marked as the Pt-edge and Se-edge, respectively. However, only one type of edge formed for AC nanoribbons (ANRs) when the $PtSe_2$ sheet was cut off along the line where Pt or Se atoms were spaced out from one other. Structural relaxations were performed for ZNRs and ANRs with different widths, which are described by the number of primitive nanoribbon cells. The optimized atomic structures of the Se-edge and Pt-edge ZNRs and ANRs with different widths are shown in Fig. 3(b). Se-edge ZNRs were not stabilized with narrow structures

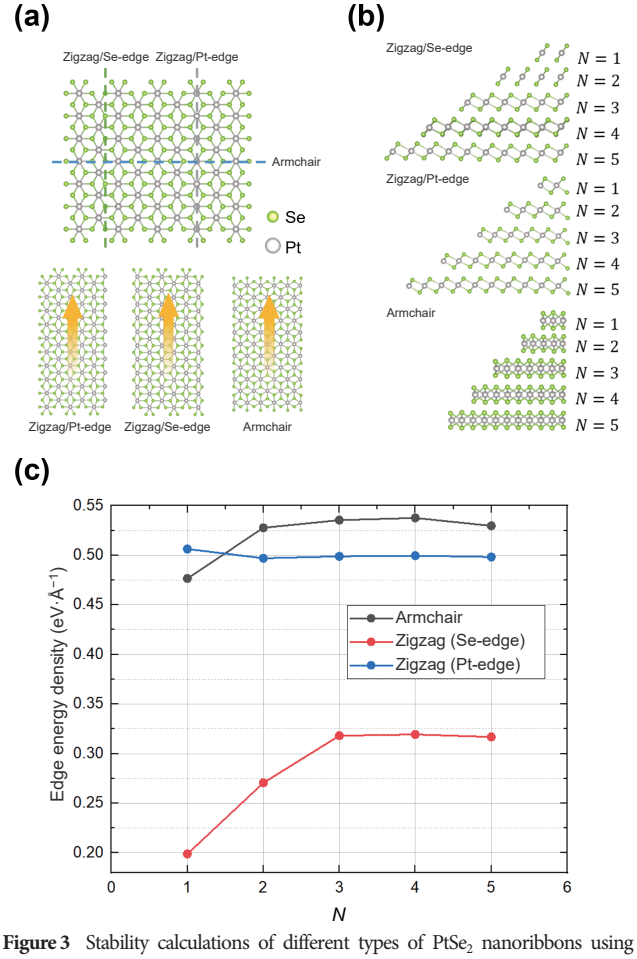

Figure 3 Stability calculations of different types of $PtSe_2$ nanoribbons using DFT. (a) Top views of $PtSe_2$ ZNRs with Pt/Se edge and ANRs. (b) Side views of different types of $PtSe_2$ nanoribbons with widths ranging from $N = 1$ to $N = 5$. (c) Edge energy density plots with respect to nanoribbon widths N.

(N = 1 and N = 2). Pt-edge ZNRs and ANRs exhibited stable atomic structures with different widths. Edge atoms were restructured with slight displacements for stabilized nanoribbon structures, which proved that $PtSe_2$ nanoribbons were stabilized by edge reconstruction, similar to other nanoribbons [43]. The edge energy (per unit length) was used to describe the stability of different types of $PtSe_2$ nanoribbons [44]. The edge energy of each type of $PtSe_2$ nanoribbon converged to a constant, indicating that the corresponding nanoribbon was stabilized, as shown in Fig. 3(c). Se-edge ZNRs presented the lowest edge energy, indicating that ZZ-oriented growth took precedence over AC-oriented growth, as shown in the experiments. To verify the universality of our edge energy analysis, the similar calculation was conducted for an analogous structure, $PtTe_2$, as shown in Fig. S10 in the ESM, demonstrating that the zigzag-Te-edge nanoribbons had the lowest edge energy.

2.4 Anisotropic electrical performance

Here, it has been elucidated that $PtSe_2$ nanoribbons exhibit anisotropic atomic structures experimentally and theoretically. It is expected that $PtSe_2$ nanoribbons should also exhibit anisotropic electrical performance. To test the anisotropic electrical performance in different directions of the $PtSe_2$ nanoribbon, electrodes were set up with channels in the ZZ (right) and AC (left) directions, as shown in Fig. 4(a). The transfer curves of the two FETs with drain-source voltage (V_{ds} = 0.1 and 1 V) for the anisotropic conductivity of $PtSe_2$ nanoribbons is shown in Fig. 4(b). The low I_{on}/I_{off} ratio (~ 1.3) reveals that $PtSe_2$ ZNRs exhibit semimetal properties [45]. Besides, the transfer characteristics of ZZ devices based on another six $PtSe_2$ nanoribbons were measured, indicating that $PtSe_2$ nanoribbon arrays exhibit the uniform electrical conductivities and semimetal properties, as shown in Figs. S11(a)–S11(f) in the ESM. The output curves of the two FETs at different temperatures, with a back-gate voltage equal to −40 V, are shown in Fig. 4(c). Empirical temperature dependence can be applied to distinguish between semiconductors and metals. Thus, the electrical conductivities of the $PtSe_2$ nanoribbons in the two directions were measured at different temperatures. However, with an increase in temperature, the monotonically increasing trends of the 2D conductivities of $PtSe_2$ ZNRs in the ZZ and AC directions revealed that the former behaved like a semiconductor, as shown in Fig. 4(d) [46]. Thus, our as-fabricated few-layer $PtSe_2$ nanoribbons were in the vicinity of the semiconductor-semimetal transition point. However, a 2D few-layer $PtSe_2$ is known as a semiconductor [46], indicating that nanoribbon shaping can contribute to the transition from semiconductor to semimetal. In order to quantify the electrical anisotropy of $PtSe_2$ nanoribbons, the ratio σ_{ZZ}/σ_{AC} was calculated with respect to temperatures, as shown in Fig. 4(e), indicating that on a large temperature scale, the conductivity of $PtSe_2$ nanoribbons in the ZZ direction was three times that in the AC

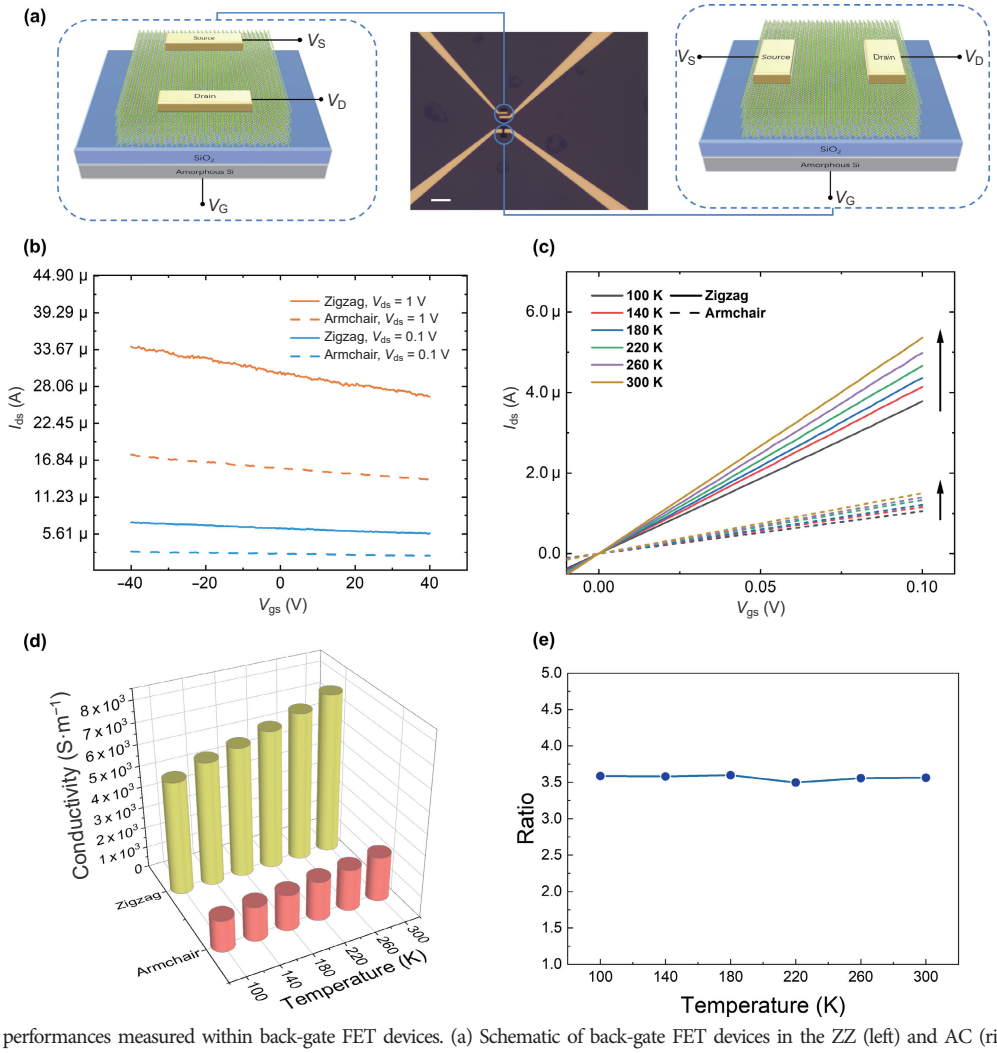

Figure 4 Electrical performances measured within back-gate FET devices. (a) Schematic of back-gate FET devices in the ZZ (left) and AC (right) directions, and optical image of back-gate FET devices on the $PtSe_2$ nanoribbon (middle). Scale bar: 10 μm. (b) Transfer curves with V_{ds} = 0.1 and 1 V. (c) Characteristic curves under different temperatures. Arrows show the direction of temperature increasing. Solid and dashed lines represent ZZ and AC, respectively. (d) Measured electrical conductivities of ZZ and AC FETs under different temperatures. (e) The ratio of measured electrical conductivities of ZZ and AC FETs from (d).

direction, which is consistent with the anisotropic structure of $PtSe_2$ nanoribbons. Such electrical anisotropy was also demonstrated in other $PtSe_2$ nanoribbon-based field effect transistors under different V_{ds}, as shown in Figs. S11(g)–S11(i) in the ESM.

2.5 Electrical performance analysis

The electrical experiments determined that the as-fabricated few-layer $PtSe_2$ nanoribbons were neither semiconductor (low I_{on}/I_{off} ratio) or semimetal (monotonically increasing trend of conductivity with increasing temperature). This implies that nanoribbon shaping is likely to render a few-layer $PtSe_2$ that is more semi-metallic. Meanwhile, the electrical performances were proven to be anisotropic, consistent with the anisotropic structures. Herein, first-principle calculations (based on DFT) and semi-classic calculations (based on Boltzmann theory) were performed to understand the underlying mechanism of the anisotropic nanoribbon-shaping few-layer $PtSe_2$. Generally, a $PtSe_2$ monolayer is recognized as a semiconductor [47]. However, the DFT calculations showed that the edge states from nanoribbon shaping reduced the bandgap of the $PtSe_2$ monolayer, rendering it more semimetal-like. The band structure and density of states (DOS) of monolayer $PtSe_2$ using DFT calculations based on Perdew, Burke, and Ernzerhof (PBE) functionals are shown in Fig. 5(a). It is known that generalized gradient approximation functionals underestimate the bandgap of semiconductors due to the lack of discontinuity in the functional derivative. However, this study focused on the change in bandgaps and energy dispersion in the vicinity of the Fermi level, for which PBE functionals are sufficient. An indirect bandgap of 1.37 eV revealed that monolayer $PtSe_2$ was a p-type semiconductor. Conversely, the bandgap decreased from 1.37 to 0.0618 eV in monolayer $PtSe_2$ ZNR (width N = 5), indicating that $PtSe_2$ nanoribbons behave more like semimetals, as shown in Figs. 5(b) and 5(c).

Projected band structures and DOS were determined for the $PtSe_2$ ZNR to understand the transformation of the bandgap. The projection to orbitals and edge atoms (from the three outermost layers) are shown in Figs. 5(b) and 5(c), respectively. The atoms on the edges contributed to the valence and conductance bands, which are attributed to Se atoms and Pt atoms, respectively, as shown in Fig. 5(b). The p_y and p_z orbitals of Se atoms and the d_{yz} orbital of Pt atoms dominated the bandgap reduction, as shown in Fig. 5(c). The wavefunctions squared of the valence and conductance bands at the X point are shown in Figs. 5(d) and 5(e), respectively. A dumbbell-like shape in the yz plane can be observed near the Se atoms on the edges, proving that the formation of the valence band is attributed to p_y and p_z orbitals localized in the vicinity of Se edge atoms. A distorted clover-like shape in the yz plane can be observed near the Pt and Se atoms on the edges, revealing that the formation of the conductance band is attributed to the coupling of Pt-d_{yz} and Se-p orbitals, as shown in Fig. 5(e). This is consistent with the orbital-projected band structures and DOS in Fig. 5(c). These results further confirm the impressive discovery of a possible transition from semiconductor to semimetal by shaping 2D flakes into 1D nanostructures.

A constant relaxation time approximation was used in the semi-classic transport calculations to explore the mechanism of anisotropic electrical performance [48]. The calculated σ/τ (ratio of electrical conductivity to relaxation time) as a function of the chemical potential at 300 K is shown in Fig. 5(f). The electrical conductivity in the ZZ direction is higher than that in the AC direction, which can be embodied in the band structures, as shown in Fig. 5(g).

The electrical conductivity can be expressed as $\sigma_{\alpha\beta}(T;\mu) =$

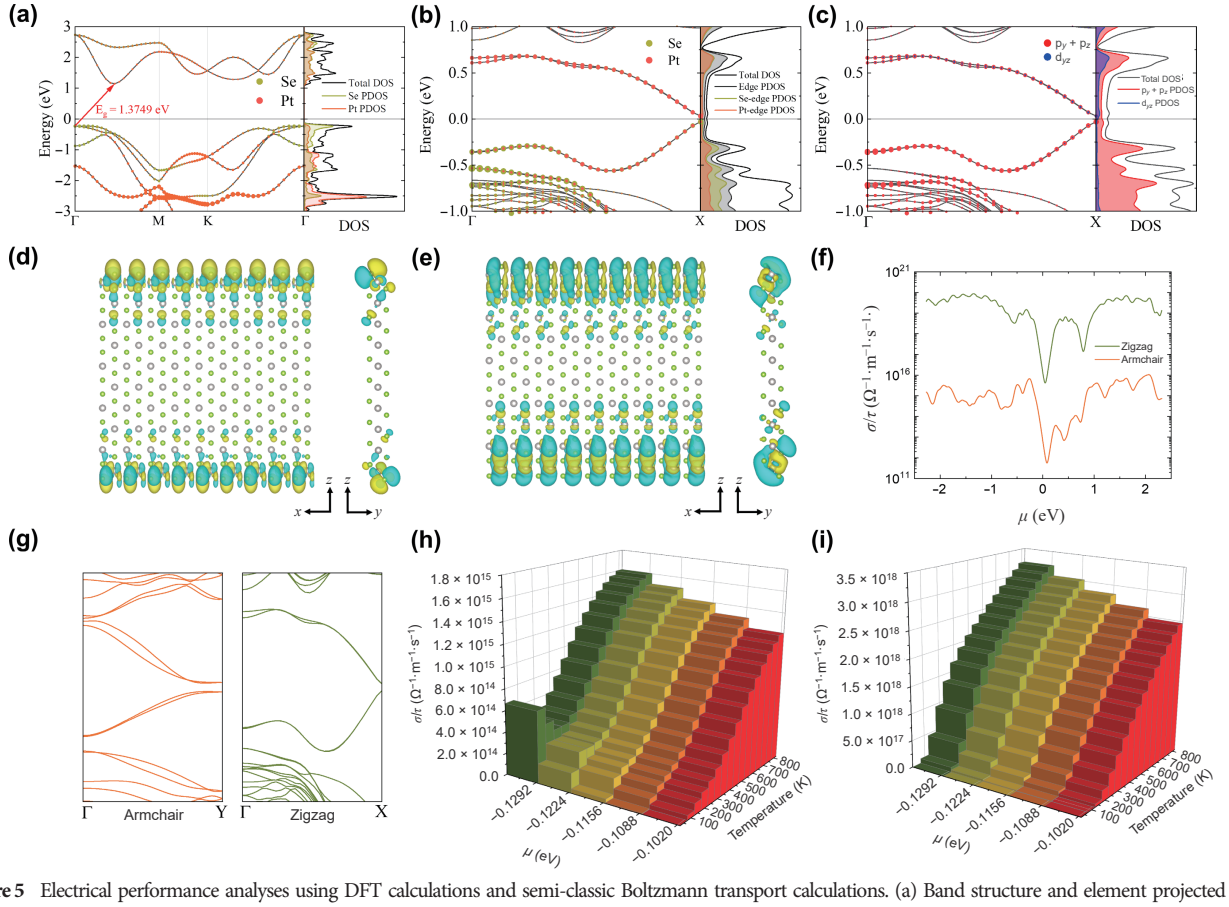

Figure 5 Electrical performance analyses using DFT calculations and semi-classic Boltzmann transport calculations. (a) Band structure and element projected DOS plots of monolayer $PtSe_2$, where the Fermi level was set to zero. (b) Atom projected and (c) orbital projected band structures and DOS plots of $PtSe_2$ ZNR. Wavefunctions squared of the (d) valence and (e) conductance bands at the X point. (f) Calculated σ/τ as a function of chemical potential at 300 K. (g) Band structures of $PtSe_2$ ANR (left) and ZNR (right). Relations of conductivities to temperature and chemical potential of $PtSe_2$ for (h) ZNR and (i) ANR.

$\frac{1}{\Omega}\int \sigma_{\alpha\beta}(\varepsilon)\left[-\frac{\partial f_\mu(T;\varepsilon)}{\partial \varepsilon}\right]d\varepsilon$, where $f_\mu(T;\varepsilon)=\frac{1}{1+\exp\left(\frac{\varepsilon-\mu}{kT}\right)}$ is the Fermi–Dirac function and $\sigma_{\alpha\beta}(\varepsilon)=\frac{1}{N}\sum_{i,k}\sigma_{\alpha\beta}(i,k)\,\delta(\varepsilon-\varepsilon_{i,k})$ is the energy projected conductivity tensor. The derivative $\left[-\frac{\partial f_\mu(T;\varepsilon)}{\partial \varepsilon}\right]$ only has a large value near the chemical potential μ, thus, the electrical conductivity is mainly derived from $\sigma_{\alpha\beta}(\varepsilon)$ near the Fermi level. The electrical conductivity tensor can be related to the group velocity using $\sigma_{\alpha\beta}(i,k)=q_e^2\tau v_\alpha(i,k)v_\beta(i,k)$, where $v_\alpha(i,k)=\frac{1}{\hbar}\frac{\partial \varepsilon_{i,k}}{\partial k_\alpha}$ is the group velocity derived from the band structure. Electrons derive large group velocities from a sharp peak/valley near the valence band maximum (VBM)/conductance band minimum (CBM) in the ZZ direction, whereas small group velocities are derived from a smooth peak/valley near the VBM/CBM in the AC direction, as shown in Fig. 5(g). Hence, the anisotropic electrical performance of the $PtSe_2$ nanoribbons can be attributed to the anisotropic derivatives at VBM/CBM. Furthermore, the temperature dependence of the electrical conductivity was also investigated, and the relationship between conductivity, temperature, and chemical potential in the ZZ and AC directions are shown in Figs. 5(h) and 5(i), respectively. The range of chemical potential was chosen in consideration of vacancy-induced p-type doping. The conductivity followed a monotonically decreasing trend with increasing chemical potential, which is consistent with the transfer curves in Fig. 4(b). The conductivity showed a monotonically increasing trend with increasing temperature, which is consistent with the experimental results, indicating a slightly semiconductor-like property.

3 Conclusion

In summary, a feasible pattern strategy was proposed to successfully fabricate aligned $PtSe_2$ nanoribbon arrays that were pre-patterned using EBL and electron-beam evaporation. The uniformity of the elemental distribution and morphology was demonstrated by systematic characterizations of SEM, EDS, HRTEM, and Raman mapping. To further study the anisotropic structures of $PtSe_2$ nanoribbons, TEM and HRTEM were conducted to explore the lattice orientations, and ARPRS was conducted to demonstrate that the $PtSe_2$ nanoribbon arrays naturally aligned in the ZZ direction. Interestingly, it was found that the anisotropic intensities of the A_{1g} mode corresponded to the anisotropic structure of the $PtSe_2$ nanoribbon. The strongest and weakest intensities corresponded to the ZZ and AC directions, respectively. DFT calculations demonstrated that ZZ $PtSe_2$ nanoribbons with Se edges had the lowest edge energy among the three nanoribbon configurations, which illustrated the underlying mechanism of orientation-selective growth of as-fabricated ZZ $PtSe_2$ nanoribbons. Additionally, back-gate FETs were constructed from as-fabricated $PtSe_2$ nanoribbons to measure the anisotropic electrical conductivity. Low I_{on}/I_{off} ratios showed a semimetal transition, whereas the increasingly monotonical conductivity dependence on temperature demonstrated that the proposed few-layer $PtSe_2$ nanoribbons were slightly semiconductor-like. Furthermore, DFT calculations revealed that edge states (coupling of Pt-d_{yz} and Se-p orbitals) dominated the semimetal transition of few-layer $PtSe_2$ nanoribbons. Anisotropic electrical conductivities were also clarified using the Boltzmann transport theory. This systematic investigation, including controllable and scalable nanoribbon production, characterization, fabrication of FET devices, electrical measurement, and theoretical analysis, paves the way for designing and fabricating electronic and optoelectronic devices based on TMD materials.

4 Methods

4.1 Production of $PtSe_2$ nanoribbons

Firstly, a polymethyl methacrylate (PMMA) layer was spin-coated onto the SiO_2/Si substrate and patterned by EBL. Then, a thin Pt film was deposited onto the substrate by electron beam evaporation to form aligned Pt nanoribbons after residual PMMA layer removed. The substrate with Pt nanoribbons was placed at the center of the tube furnace, where elemental selenium powder (99.99% purity) were placed at the upstream side and evaporated at 220 °C. The selenium steam was brought to the substrate by 50 SCCM N_2 flow and the substrate was heated to 420 °C for 1 h. After the natural cooling to room temperature, aligned $PtSe_2$ nanoribbons were obtained.

4.2 Characterization of the $PtSe_2$ nanoribbons

SEM and corresponding EDS mapping were conducted using a Mira3 LMH instrument (TESCAN). The TEM images were obtained using an H-7650B microscope at 80 kV. HRTEM images and mappings were acquired using a JEM-2100F analytical electron microscope at 200 kV. XRD patterns were obtained using a Bruker D8 Advance XRD-7000 diffractometer with Cu Kα radiation (λ = 1.54178 Å) at 5° to 80° scanning angles. Micro-zone XPS spectra of $PtSe_2$ nanoribbons on the substrate were obtained with a PHI Quantera II system using Al Kα as the excitation source. Raman spectra and polarized Raman spectra were collected using a Horiba–Jobin–Yvon Raman system under 532 nm laser excitation with 5% power (0.65 mW). AFM was performed using a Bruker Dimension Icon instrument.

4.3 Device fabrication and measurement

A bottom-gated field effect transistor structure with highly p-doped Si as bottom gate and 90-nm thick SiO_2 as gate insulator was fabricated to investigate the anisotropic properties of $PtSe_2$ nanoribbons. Source/drain electrodes were patterned by EBL and deposited with Cr/Au (5 nm/50 nm) to form the contact. It was noted that devices for characterizing zigzag and armchair conductivity were fabricated with the same width and length and based on the same nanoribbon. The electrical performance was measured by an Agilent B1500A semiconductor parameter analyzer with a variable temperature probe station ranging from 100 to 300 K at vacuum atmosphere.

4.4 First-principle calculations

All DFT calculations were conducted using the Vienna *ab initio* simulation package (VASP) [49–52]. The generalized gradient approximation (GGA) as parameterized by PBE was used to describe the exchange–correlation interactions [53]. The electron–ion interactions were described by the projector-augmented wave (PAW) pseudopotentials [54, 55]. The cutoff energy of the plane wave expansion was set to 400 eV. Monkhorst–Pack grid with a spacing of 0.04 × 2π Å^{-1} was used to perform the Brillouin Zone sampling [56]. The thresholds for the total energy convergence was set to 10^{-8} eV and the crystal geometry was optimized until the atomic forces become less than 0.01 eV/Å. To avoid the interactions between periodic images of nanoribbons, vacuum slabs of 15 Å were set up in the y and z directions. The semi-classic Boltzmann transport equation calculations were performed using the BoltzTraP code [48]. The edge energy (per unit length) is defined as $E_{edge}=(E_{NR}-NE_{atom})/2L$, where E_{NR} is the total energy of the optimized nanoribbons, E_{atom} is the average energy of each atom in the optimized $PtSe_2$ bulk structure, N is the atom number in nanoribbons, and L is the length of the nanoribbons.

Acknowledgements

The authors are grateful for the financial support from the National Natural Science Foundation of China (Nos. 52072204 and 62104017), the National Postdoctoral Program for Innovative Talents of China (No. BX20200049), and China Postdoctoral Science Foundation (No. 2021M690013). We also acknowledge the Tsinghua Xuetang Talents Program for providing the computational resources.

Electronic Supplementary Material: Supplementary material (optical images of the substrate with Pt arrays, and patterned $PtSe_2$ arrays; characterizations of $PtSe_2$ nanoribbon arrays, including HRTEM, Raman mapping, Raman spectra, and XPS) is available in the online version of this article at https://doi.org/10.1007/s12274-022-4110-3.

References

[1] Wang, Q. H.; Kalantar-Zadeh, K.; Kis, A.; Coleman, J. N.; Strano, M. S. Electronics and optoelectronics of two-dimensional transition metal dichalcogenides. *Nat. Nanotechnol.* **2012**, *7*, 699–712.

[2] Li, X. F.; Yang, L. M.; Si, M. W.; Li, S. C.; Huang, M. Q.; Ye, P. D.; Wu, Y. Q. Performance potential and limit of MoS_2 transistors. *Adv. Mater.* **2015**, *27*, 1547–1552.

[3] Zhou, H. L.; Wang, C.; Shaw, J. C.; Cheng, R.; Chen, Y.; Huang, X. Q.; Liu, Y.; Weiss, N. O.; Lin, Z. Y.; Huang, Y. et al. Large area growth and electrical properties of p-type WSe_2 atomic layers. *Nano Lett.* **2015**, *15*, 709–713.

[4] Das, P. K.; Di Sante, D.; Vobornik, I.; Fujii, J.; Okuda, T.; Bruyer, E.; Gyenis, A.; Feldman, B. E.; Tao, J.; Ciancio, R. et al. Layer-dependent quantum cooperation of electron and hole states in the anomalous semimetal WTe_2. *Nat. Commun.* **2016**, *7*, 10847.

[5] Hsu, C.; Frisenda, R.; Schmidt, R.; Arora, A.; De Vasconcellos, S. M.; Bratschitsch, R.; Van Der Zant, H. S. J.; Castellanos-Gomez, A. Thickness-dependent refractive index of 1L, 2L, and 3L MoS_2, $MoSe_2$, WS_2, and WSe_2. *Adv. Opt. Mater.* **2019**, *7*, 1900239.

[6] Camellini, A.; Mennucci, C.; Cinquanta, E.; Martella, C.; Mazzanti, A.; Lamperti, A.; Molle, A.; De Mongeot, F. B.; Valle, G. D.; Zavelani-Rossi, M. Ultrafast anisotropic exciton dynamics in nanopatterned MoS_2 sheets. *ACS Photonics* **2018**, *5*, 3363–3371.

[7] Kolobov, A. V.; Fons, P.; Tominaga, J. Electronic excitation-induced semiconductor-to-metal transition in monolayer $MoTe_2$. *Phys. Rev. B Condens. Matter.* **2016**, *94*, 094114.

[8] Ma, H. F.; Qian, Q.; Qin, B.; Wan, Z.; Wu, R. X.; Zhao, B.; Zhang, H. M.; Zhang, Z. C.; Li, J.; Zhang, Z. W. et al. Controlled synthesis of ultrathin $PtSe_2$ nanosheets with thickness-tunable electrical and magnetoelectrical properties. *Adv. Sci.* **2021**, 2103507.

[9] Hu, H. W.; Wang, H. P.; Sun, Y. L.; Li, J. W.; Wei, J. L.; Xie, D.; Zhu, H. W. Out-of-plane and in-plane ferroelectricity of atom-thick two-dimensional InSe. *Nanotechnology* **2021**, *32*, 385202.

[10] Sun, M. X.; Fang, Q. Y.; Xie, D.; Sun, Y. L.; Qian, L.; Xu, J. L.; Xiao, P.; Teng, C. J.; Li, W. W.; Ren, T. L. et al. Heterostructured graphene quantum dot/WSe_2/Si photodetector with suppressed dark current and improved detectivity. *Nano Res.* **2018**, *11*, 3233–3243.

[11] Lee, D.; Hwang, E.; Lee, Y.; Choi, Y.; Kim, J. S.; Lee, S.; Cho, J. H. Multibit MoS_2 photoelectronic memory with ultrahigh sensitivity. *Adv. Mater.* **2016**, *28*, 9196–9202.

[12] Lin, Z. Y.; Liu, Y.; Halim, U.; Ding, M. N.; Liu, Y. Y.; Wang, Y. L.; Jia, C. C.; Chen, P.; Duan, X. D.; Wang, C. et al. Solution-processable 2D semiconductors for high-performance large-area electronics. *Nature* **2018**, *562*, 254–258.

[13] Ge, J.; Luo, T. C.; Lin, Z. Z.; Shi, J. P.; Liu, Y. Z.; Wang, P. Y.; Zhang, Y. F.; Duan, W. H.; Wang, J. Magnetic moments induced by atomic vacancies in transition metal dichalcogenide flakes. *Adv. Mater.* **2021**, *33*, 2005465.

[14] Arab, A.; Li, Q. L. Anisotropic thermoelectric behavior in armchair and zigzag mono- and fewlayer MoS_2 in thermoelectric generator applications. *Sci. Rep.* **2015**, *5*, 13706.

[15] Ataca, C.; Şahin, H.; Aktürk, E.; Ciraci, S. Mechanical and electronic properties of MoS_2 nanoribbons and their defects. *J. Phys. Chem. C* **2011**, *115*, 3934–3941.

[16] Soleimani-Amiri, S.; Rudi, S. G. Effects of sulfur line vacancy defects on the electronic and optical properties of armchair MoS_2 nanoribbon. *Opt. Mater.* **2020**, *110*, 110491.

[17] Tong, L.; Duan, X. Y.; Song, L. Y.; Liu, T. D.; Ye, L.; Huang, X. Y.; Wang, P.; Sun, Y. H.; He, X.; Zhang, L. J. et al. Artificial control of in-plane anisotropic photoelectricity in monolayer MoS_2. *Appl. Mater. Today* **2019**, *15*, 203–211.

[18] Xia, F. N.; Wang, H.; Jia, Y. C. Rediscovering black phosphorus as an anisotropic layered material for optoelectronics and electronics. *Nat. Commun.* **2014**, *5*, 4458.

[19] Qiao, J. S.; Kong, X. H.; Hu, Z. X.; Yang, F.; Ji, W. High-mobility transport anisotropy and linear dichroism in few-layer black phosphorus. *Nat. Commun.* **2014**, *5*, 4475.

[20] Dolui, K.; Pemmaraju, C. D.; Sanvito, S. Electric field effects on armchair MoS_2 nanoribbons. *ACS Nano* **2012**, *6*, 4823–4834.

[21] Pan, J.; Wang, R.; Zhou, X. Y.; Zhong, J. S.; Xu, X. Y.; Hu, J. G. Transition-metal doping induces the transition of electronic and magnetic properties in armchair MoS_2 nanoribbons. *Phys. Chem. Chem. Phys.* **2017**, *19*, 24594–24604.

[22] Nayeri, M.; Fathipour, M. A numerical analysis of electronic and optical properties of the zigzag MoS_2 nanoribbon under uniaxial strain. *IEEE Trans. Electron Devices* **2018**, *65*, 1988–1994.

[23] Feng, X. W.; Huang, X.; Chen, L.; Tan, W. C.; Wang, L.; Ang, K. W. High mobility anisotropic black phosphorus nanoribbon field-effect transistor. *Adv. Funct. Mater.* **2018**, *28*, 1801524.

[24] Zhao, Y. S.; Zhang, G.; Nai, M. H.; Ding, G. Q.; Li, D. F.; Liu, Y.; Hippalgaonkar, K.; Lim, C. T.; Chi, D. Z.; Li, B. W. et al. Probing the physical origin of anisotropic thermal transport in black phosphorus nanoribbons. *Adv. Mater.* **2018**, *30*, 1804928.

[25] Yim, C.; Lee, K.; McEvoy, N.; O'Brien, M.; Riazimehr, S.; Berner, N. C.; Cullen, C. P.; Kotakoski, J.; Meyer, J. C.; Lemme, M. C. et al. High-performance hybrid electronic devices from layered $PtSe_2$ films grown at low temperature. *ACS Nano* **2016**, *10*, 9550–9558.

[26] Liu, Z. F.; Sun, Y. L.; Cao, H. Q.; Xie, D.; Li, W.; Wang, J. O.; Cheetham, A. K. Unzipping of black phosphorus to form zigzag-phosphorene nanobelts. *Nat. Commun.* **2020**, *11*, 3917.

[27] Watts, M. C.; Picco, L.; Russell-Pavier, F. S.; Cullen, P. L.; Miller, T. S.; Bartuś, S. P.; Payton, O. D.; Skipper, N. T.; Tileli, V.; Howard, C. A. Production of phosphorene nanoribbons. *Nature* **2019**, *568*, 216–220.

[28] Xie, C.; Zeng, L. H.; Zhang, Z. X.; Tsang, Y. H.; Luo, L. B.; Lee, J. H. High-performance broadband heterojunction photodetectors based on multilayered $PtSe_2$ directly grown on a Si substrate. *Nanoscale* **2018**, *10*, 15285–15293.

[29] Zhao, Y. D.; Qiao, J. S.; Yu, Z. H.; Yu, P.; Xu, K.; Lau, S. P.; Zhou, W.; Liu, Z.; Wang, X. R.; Ji, W. et al. High-electron-mobility and air-stable 2D layered $PtSe_2$ FETs. *Adv. Mater.* **2017**, *29*, 1604230.

[30] Zeng, L. H.; Lin, S. H.; Li, Z. J.; Zhang, Z. X.; Zhang, T. F.; Xie, C.; Mak, C. H.; Chai, Y.; Lau, S. P.; Luo, L. B. et al. Fast, self-driven, air-stable, and broadband photodetector based on vertically aligned $PtSe_2$/GaAs heterojunction. *Adv. Funct. Mater.* **2018**, *28*, 1705970.

[31] Jiang, W.; Wang, X. D.; Chen, Y.; Wu, G. J.; Ba, K.; Xuan, N. N.; Sun, Y. Y.; Gong, P.; Bao, J. X.; Shen, H. et al. Large-area high quality $PtSe_2$ thin film with versatile polarity. *InfoMat* **2019**, *1*, 260–267.

[32] Avsar, A.; Cheon, C. Y.; Pizzochero, M.; Tripathi, M.; Ciarrocchi, A.; Yazyev, O. V.; Kis, A. Probing magnetism in atomically thin semiconducting $PtSe_2$. *Nat. Commun.* **2020**, *11*, 4806.

[33] Yao, W.; Wang, E. Y.; Huang, H. Q.; Deng, K.; Yan, M. Z.; Zhang, K. N.; Miyamoto, K.; Okuda, T.; Li, L. F.; Wang, Y. L. et al. Direct observation of spin-layer locking by local Rashba effect in monolayer semiconducting $PtSe_2$ film. *Nat. Commun.* **2017**, *8*, 14216.

[34] Yan, M. Z.; Wang, E. Y.; Zhou, X.; Zhang, G. Q.; Zhang, H. Y.; Zhang, K. N.; Yao, W.; Lu, N. P.; Yang, S. Z.; Wu, S. L. et al. High quality atomically thin $PtSe_2$ films grown by molecular beam epitaxy. *2D Mater.* **2017**, *4*, 045015.

[35] Gong, Y. N.; Lin, Z. T.; Chen, Y. X.; Khan, Q.; Wang, C.; Zhang, B.; Nie, G. H.; Xie, N.; Li, D. L. Two-dimensional platinum

diselenide: Synthesis, emerging applications, and future challenges. *Nano-Micro Lett.* **2020**, *12*, 174.

[36] Ping, X. F.; Liang, D.; Wu, Y. Y.; Yan, X. X.; Zhou, S. X.; Hu, D. K.; Pan, X. Q.; Lu, P. F.; Jiao, L. Y. Activating a two-dimensional $PtSe_2$ basal plane for the hydrogen evolution reaction through the simultaneous generation of atomic vacancies and Pt clusters. *Nano Lett.* **2021**, *21*, 3857–3863.

[37] Van Der Zande, A. M.; Huang, P. Y.; Chenet, D. A.; Berkelbach, T. C.; You, Y. M.; Lee, G. H.; Heinz, T. F.; Reichman, D. R.; Muller, D. A.; Hone, J. C. Grains and grain boundaries in highly crystalline monolayer molybdenum disulphide. *Nat. Mater.* **2013**, *12*, 554–561.

[38] O'Brien, M.; McEvoy, N.; Motta, C.; Zheng, J. Y.; Berner, N. C.; Kotakoski, J.; Elibol, K.; Pennycook, T. J.; Meyer, J. C.; Yim, C. et al. Raman characterization of platinum diselenide thin films. *2D Mater.* **2016**, *3*, 021004.

[39] Loudon, R. The Raman effect in crystals. *Adv. Phys.* **2001**, *50*, 813–864.

[40] Zhao, Y. D.; Qiao, J. S.; Yu, P.; Hu, Z. X.; Lin, Z. Y.; Lau, S. P.; Liu, Z.; Ji, W.; Chai, Y. Extraordinarily strong interlayer interaction in 2D layered PtS_2. *Adv. Mater.* **2016**, *28*, 2399–2407.

[41] Azizimanesh, A.; Peña, T.; Sewaket, A.; Hou, W. H.; Wu, S. M. Uniaxial and biaxial strain engineering in 2D MoS_2 with lithographically patterned thin film stressors. *Appl. Phys. Lett.* **2021**, *118*, 213104.

[42] Liu, L. N.; Wu, J. X.; Wu, L. Y.; Ye, M.; Liu, X. Z.; Wang, Q.; Hou, S. Y.; Lu, P. F.; Sun, L. F.; Zheng, J. Y. et al. Phase-selective synthesis of 1T′ MoS_2 monolayers and heterophase bilayers. *Nat. Mater.* **2018**, *17*, 1108–1114.

[43] Chen, K. Y.; Deng, J. K.; Ding, X. D.; Sun, J.; Yang, S.; Liu, J. Z. Ferromagnetism of 1T′-MoS_2 nanoribbons stabilized by edge reconstruction and its periodic variation on nanoribbons width. *J. Am. Chem. Soc.* **2018**, *140*, 16206–16212.

[44] Gan, C. K.; Srolovitz, D. J. First-principles study of graphene edge properties and flake shapes. *Phys. Rev. B Condens. Matter.* **2010**, *81*, 125445.

[45] Ansari, L.; Monaghan, S.; McEvoy, N.; Coileáin, C. Ó.; Cullen, C. P.; Lin, J.; Siris, R.; Stimpel-Lindner, T.; Burke, K. F.; Mirabelli, G. et al. Quantum confinement-induced semimetal-to-semiconductor evolution in large-area ultra-thin $PtSe_2$ films grown at 400 °C. *npj 2D Mater. Appl.* **2019**, *3*, 33.

[46] Wang, L.; Zhang, S. F.; McEvoy, N.; Sun, Y. Y.; Huang, J. W.; Xie, Y. F.; Dong, N. N.; Zhang, X. Y.; Kislyakov, I. M.; Nunzi, J. M. et al. Nonlinear optical signatures of the transition from semiconductor to semimetal in $PtSe_2$. *Laser Photon. Rev.* **2019**, *13*, 1900052.

[47] Kandemir, A.; Akbali, B.; Kahraman, Z.; Badalov, S. V.; Ozcan, M.; Iyikanat, F.; Sahin, H. Structural, electronic and phononic properties of $PtSe_2$: From monolayer to bulk. *Semicond. Sci. Technol.* **2018**, *33*, 085002.

[48] Madsen, G. K. H.; Singh, D. J. BoltzTraP. A code for calculating band-structure dependent quantities. *Comput. Phys. Commun.* **2006**, *175*, 67–71.

[49] Kresse, G.; Furthmüller, J. Efficient iterative schemes for *ab initio* total-energy calculations using a plane-wave basis set. *Phys. Rev. B Condens. Matter.* **1996**, *54*, 11169–11186.

[50] Kresse, G.; Furthmüller, J. Efficiency of *ab-initio* total energy calculations for metals and semiconductors using a plane-wave basis set. *Comput. Mater. Sci.* **1996**, *6*, 15–50.

[51] Kresse, G.; Hafner, J. *Ab initio* molecular-dynamics simulation of the liquid–metal–amorphous–semiconductor transition in germanium. *Phys. Rev. B Condens. Matter.* **1994**, *49*, 14251–14269.

[52] Kresse, G.; Hafner, J. *Ab initio* molecular dynamics for liquid metals. *Phys. Rev. B Condens. Matter.* **1993**, *47*, 558–561.

[53] Perdew, J. P.; Burke, K.; Ernzerhof, M. Generalized gradient approximation made simple. *Phys. Rev. Lett.* **1996**, *77*, 3865–3868.

[54] Kresse, G.; Joubert, D. From ultrasoft pseudopotentials to the projector augmented-wave method. *Phys. Rev. B Condens. Matter.* **1999**, *59*, 1758–1775.

[55] Blöchl, P. E. Projector augmented-wave method. *Phys. Rev. B Condens. Matter.* **1994**, *50*, 17953–17979.

[56] Monkhorst, H. J.; Pack, J. D. Special points for brillouin-zone integrations. *Phys. Rev. B Condens. Matter.* **1976**, *13*, 5188–5192.